RESEARCH ARTICLE | AUGUST 12 2024

Complex network analysis of a premixed swirling flame influenced by precessing vortex core ⊘

Yongzhi Ren (任勇智) ; Qiuxiao Wang (汪秋笑) ; Yu Guan (关昱) ; Xi Xia (夏溪) ✉ ; Fei Qi (齐飞) ✉

Check for updates

View Online

Export Citation

Articles You May Be Interested In

Influence of inner shear layer on the emergence of central recirculation zone in a V-shaped premixed swirling flame

Physics of Fluids (October 2023)

Effects of the fresh mixture temperature on thermoacoustic instabilities in a lean premixed swirl-stabilized combustor

Physics of Fluids (April 2020)

Numerical modeling and suppression of combustion instabilities in a partially premixed combustor

Physics of Fluids (September 2024)

Complex network analysis of a premixed swirling flame influenced by precessing vortex core

View Online　Export Citation　CrossMark

Yongzhi Ren (任勇智),[1] (iD) Qiuxiao Wang (汪秋笑),[1] (iD) Yu Guan (关昱),[2] (iD) Xi Xia (夏溪),[1,a] (iD) and Fei Qi (齐飞)[1,a] (iD)

AFFILIATIONS

[1]School of Mechanical Engineering, Shanghai Jiao Tong University, Shanghai 200240, People's Republic of China
[2]Department of Aeronautical and Aviation Engineering, The Hong Kong Polytechnic University, Kowloon, Hong Kong

[a]Authors to whom correspondence should be addressed: xiaxiss@sjtu.edu.cn and fqi@sjtu.edu.cn

ABSTRACT

This work investigates the influences of precessing vortex cores (PVCs) on the coherent interactions in the transient flow and heat release fields of a weak premixed swirling flame, based on a 10-kHz simultaneous measurement of OH* chemiluminescence and stereoscopic particle image velocimetry together with the state-of-the-art vortical and heat release rate (HRR) network analyses. The PVC effect is studied by contrasting the lifted helical and attached symmetric states of a unique transitioning V-shaped flame, corresponding to an alternate quasi-periodic appearance and disappearance of PVC in the inner shear layer (ISL). The results suggest that the emergence of PVC significantly escalates the coherent oscillation in the ISL, leading to the break of the scale-free topology in the vortical network. However, the PVC also promotes coherence in the local HRR variation, resulting in improved connectivity in the positive HRR network and enhanced assortative mixing in the negative HRR network. Furthermore, the flame mode transition is also captured by the differences in the mean degree of the positive HRR network and the power-law fitting goodness of the negative HRR network, showing promises of complex network analysis in distinguishing the flame dynamical modes.

Published under an exclusive license by AIP Publishing. https://doi.org/10.1063/5.0215162

I. INTRODUCTION

Swirl combustion is prevalently utilized in aero-engine combustors to generate a large-scale recirculation zone with high temperature, promoting the heating of upstream premixture and flame stabilization.[1,2] The lean premixed techniques[1,3–5] have been developed to achieve reduced NOx emissions[6] in swirl combustion as a response to the increasingly stringent environmental regulations.[1] However, the flow and flame in this combustion regime could be susceptible to instabilities induced by hydrodynamic or acoustic perturbations. Particularly, the main vortices formed in shear layers have a direct impact on flame dynamics, serving as a prominent source of flame instability.[7–9] Furthermore, vortices emanating from the injector lip can lead to deformation, cusp formation, and roll-up of flame surfaces, causing variations in heat release rate (HRR) and altering flame response to external forcing.[8,10] Conversely, the heat release could also influence the formation and shedding of the vortices in the outer shear layer.[11]

Among various vortical structures, the precessing vortex core (PVC) has garnered significant attention due to its highly asymmetric and quasi-periodic patterns observed in both reacting and non-reacting conditions.[12–14] PVC is a spiral-shaped vortex displaced from the central axis and is characterized by a precession movement. From a hydrodynamic view, PVC is a manifestation of self-excited hydrodynamic instability in the helical mode, which can substantially impact the flame dynamics by altering the large-scale flame structures and their motions.[15–17] Previous studies[12,17–21] have utilized linear stability analysis (LSA) to predict the frequency and growth rate of PVC, successfully capturing its helical evolution and its influence on flame dynamics.[12,19,22–27] Stöhr *et al.*[28] explored the lift-up dynamics of partially premixed swirling flames and established a connection between the PVC behavior and local extinction. An *et al.*[23,29] investigated the coupling dynamics between PVC and flame shape transition. They proposed that PVC forms before flame lifting, subsequently increasing the strain rate at the flame root and resulting in complete flame detachment from the nozzle. Stöhr *et al.*[19] asserted that PVC plays a pivotal role in the flame detachment process by creating an unsteady stagnation point that destabilizes the flame root. Furthermore, they employed transient LSA based on data in the literature[12] and revealed that PVC suppression primarily results from thermoacoustic instability, which modifies the mean flow field. Interestingly, PVC can act as either a suppressor or a trigger of thermoacoustic instability. On the one hand, PVC could suppress the thermo-acoustic instabilities by

enhancing local mixing to mitigate the local equivalence ratio fluctuation[30] or reducing the shear layer receptivity to external longitudinal forcing.[31] On the other hand, the helical evolution of PVC could enhance local turbulence,[32] which could potentially cause HRR oscillations by imposing velocity disturbances onto the flame surface.[33,34] Under some particular conditions, PVC formed by helical flow instability could directly couple with thermoacoustic oscillations[25,35,36] and enhance the acoustically coupled HRR fluctuation,[37] thereby serving as a potential trigger for thermoacoustic instabilities.[38] In addition, PVC can also promote rapid fuel-air mixing and reduce emissions of both NOx and carbon monoxide.[39] Thus, understanding the dynamics of PVC and its induced flame instability is crucial to developing the swirl combustion technique.

Fostered by the advancement in computational capabilities and the availability of high-speed laser diagnostics, novel data-driven approaches[18,40–42] have been developed to interpret coherent dynamics in swirling flows. Among them, complex network theory has become increasingly popular in analyzing the spatiotemporal behavior of diverse systems in nonreacting[43,44] and reacting[45,46] flows. Given its unique capability to highlight interactions and connectivity among a large group of elements, complex network theory offers a refreshing perspective to analyze fluid dynamics where interactions play important roles. Based on the measured time-series signals, the method of visibility graphs enables the identification of the pattern during the transition from combustion noise to thermoacoustic instability.[47,48] Nair and Taira[49] and Taira et al.[50] utilized the sparse approximation of a weighted vortical network to study vortex–vortex interaction dynamics and found the scale-free feature of decaying isotropic turbulence. Kasthuri et al.[51] constructed positively and negatively correlated weighted networks from CH* chemiluminescence intensity for different dynamical states during the transition to thermoacoustic instability. They found that network measures quantitatively capture the extent of coherence in the flame dynamics. Rywik et al.[52] combined the vortical and HRR networks to analyze the spatiotemporal dynamics of swirl flames under various hydrogen–methane fuel blends, showing that the scale-free topology of the vortical network only exists in the absence of hydrogen enrichment while the HRR network is responsive to hydrogen concentration and acoustic pressure amplitude.

Recently, the authors and collaborators adopted the vortical network to explore the scale-free topology in turbulent swirling flames.[53] Using time-resolved vorticity data, time-varying weighted spatial vortical networks were constructed, with the node strength distribution derived from the Biot–Savart law.[49,50] The results show that the most coherent flow structures act as the primary network hubs so that scale-free topology existence in the vortical networks continuously persists even after the onset of combustion instability. This discovery provides important implications for combustion instability control through destroying primary hub structures of vortical networks.

In this work, in an attempt to continue our exploration of the complex network analysis in understanding vortex–flame interaction in swirl combustion, we take one step further to examine the helical flame mode and the effect of PVC on both vortical and HRR networks, based on 10-kHz simultaneous stereoscopic particle image velocimetry (SPIV)-OH* measurement. The combined analysis of the vortical and HRR networks enables us to distinguish core spatial regions dictating the vortex–flame coupling mechanism, further shedding light on the significant role of PVC in shaping the network structures.

II. EXPERIMENTAL METHOD

In this experiment, we employ a radial swirl burner to form an unconfined swirling flame under atmospheric conditions, as depicted in Fig. 1(a). The methane–air premixture first enters the plenum chamber (130 mm in diameter and 120 mm in height) and then passes through a divergent annular duct with a continuously reduced cross-sectional area. This radial flow expansion ensures that the premixed gas interacts with the radial swirler at a deliberately subdued velocity to further suppress flow separation. The swirler configuration comprises thirty vanes of the NACA-9615 airfoil shape, each with a chord length of 30 mm. The leading edge angle of the vane is aligned with the incoming flow, as illustrated in Fig. 1(b). The swirl number (S) of the burner is calculated to be 0.38 ± 0.02 based on transverse flow-field
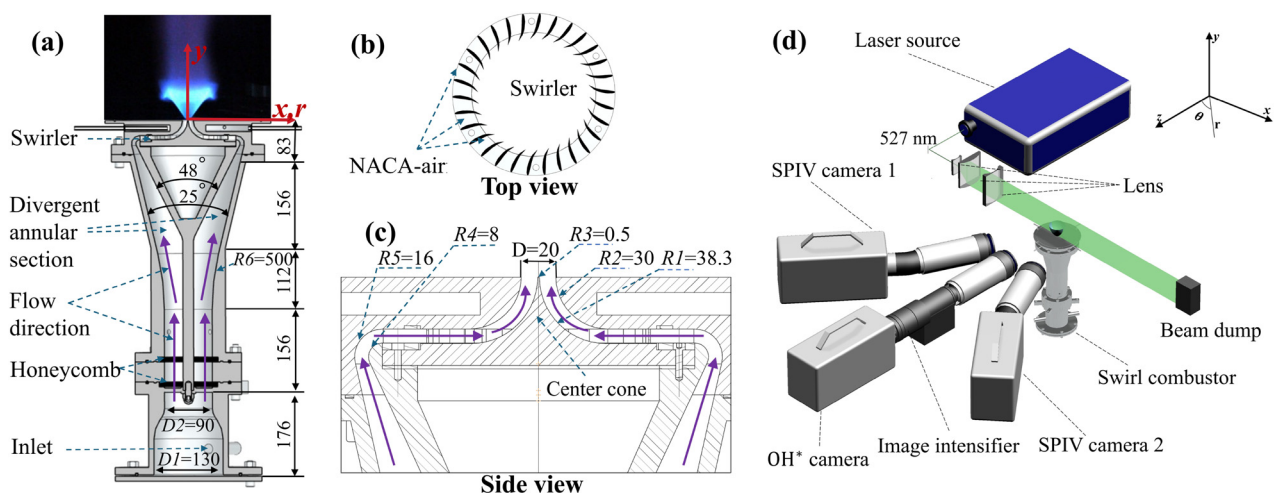
FIG. 1. (a) Schematic design of the swirl burner, (b) top view of the swirler, and (c) side view of the combustor exit nozzle with a sphere bluff body located at nozzle exit plane; and (d) laser diagnostic system of the SPIV-OH* simultaneous measurement.

data acquired at the horizontal cross section located at $y = 2\,mm$.[54] Subsequently, the swirling flow accelerates as it converges radially and turns vertically through an axisymmetric central cone before exiting the nozzle. This converging nozzle design also minimizes the risk of flashback and explosion.[55,56]

The air and fuel flows are controlled separately by two mass flow rate controllers (SevenStar CS200 series), giving the present operating conditions of Reynolds number (Re) between 2000 and 8000 and equivalence ratio (Φ) between 0.5 and 3.0. Here, $Re = UD/\nu$ is defined based on the bulk velocity (U) at the nozzle exit, the exit diameter (D), and the kinematic viscosity (ν) of the fresh mixture. While equivalent ratio Φ is calculated based on the stoichiometric air-to-fuel mass ratio ($\Phi = S_{toic}m_f/m_a$, $S_{toic} = 17.11$ for methane/air combustion), and the mass flow rates of fuel (m_f) and air (m_a). The mass flow rate controllers correspond to a measurement error of 1%, based on which the maximum uncertainties of Re and Φ are estimated to be 2.74% and 1.61%, respectively.

The optical measurement system is shown in Fig. 1(d), consisting of a dual-cavity Nd:YLF laser (Beamtech Vlite-Hi-527), outputting a 527 nm laser beam at 3.1 mJ/pulse with a repetition rate of up to 10 kHz. Two high-speed CMOS cameras (Phantom V2012) were used for SPIV imaging, while another high-speed camera (Phantom VEO1310L) was used for capturing the OH[*] chemiluminescence signal. Each SPIV camera was equipped with a Nikkor lens (Nikkor 50 mm f/1.4G) and a short bandpass filter (Edmund Optics 527/20 nm), together with a Scheimpflug adapter to make sure the SPIV cameras could meet the Scheimpflug principle to reduce tangential distortion.[57] Two SPIV cameras are located symmetrically with a viewing angle of 26° to the normal direction of the laser sheet. Aluminum oxide particles with a diameter of $\sim$1 μm are employed for flow seeding whose Stokes number is below 0.023 yielding acceptable traceability for SPIV measurements. Particle images for SPIV measurements were recorded at 10 000 fps, with a field-of-view (FOV) of about $110 \times 70\,mm^2$ and a resolution of $\sim$88 μm/pixel. Self-calibration was conducted to correct misalignment between the laser sheet and calibration plate.[58] Then, a multi-scale cross correlation SPIV algorithm (LaVision Davis 8.4) was adopted to compute the three-component velocity field in the measurement plane, with a final interrogation window of 24×24 pixels and a 75% overlap to generate a flow-field resolution of 0.53 mm/point. The uncertainties associated with in-plane and out-of-plane velocity components are estimated to be $\pm$0.019 and $\pm$0.037 m/s, respectively. Furthermore, the OH[*] chemiluminescence signal was simultaneously recorded by the OH[*] camera attached with an intensifier (Lambert Hi-CATT) and a short bandpass filter (Edmund Optics, 310/10 nm). This work involves both Cartesian and cylindrical coordinates, (x, y, z) and (r, θ, z), as shown in Fig. 1(d), with both origins positioned at the center of the nozzle exit.

III. COMPLEX NETWORK MODELING

A. Vortical network

The vortical network aims to capture the relation between vortical structures in the flow domain and identify their most influencing locations. It was shown to be able to distinguish between different dynamical states and highlight structures crucial to maintaining thermoacoustic instability.[59,60] The present vortical network follows the framework employed in our previous study.[53] The key correlation in this network, the node strength, is quantified based on the induced

velocity at each grid cell (node j) due to the vorticity present at another grid cell (node i). Thus, the induced velocity $u_{i\to j}$ at position x_j due to vorticity ω present at x_i can be calculated using the Biot–Savart law as follows:[50,53]

$$u_{i\to j} = \frac{\left|\omega(x_i, t)\Delta x \Delta y\right|}{2\pi|x_i - x_j|}, \quad (1)$$

where Δx and Δy are the grid resolution in the x and y directions, respectively. The value of Eq. (1) is finite only if i and j are different. The adjacency matrix A_v of the vortical network is defined as

$$A_{v_{ij}}(t) = \begin{cases} \frac{1}{2}(u_{i\to j} + u_{j\to i}), & \text{if } i \neq j, \\ 0, & \text{if } i = j. \end{cases} \quad (2)$$

The resultant network is undirected and includes no self-loops, as the adjacency matrix A_v is symmetric and the diagonal entries are all zeros. The adjacency matrix A_v can be constructed using vorticity evaluated from the SPIV data after cropping off the edges to remove the measurement artifacts at the window boundaries. Note that the vortical network is a time-varying network.

B. Heat release rate network

The HRR network uses correlation measures to capture the coherence of the reactive field.[51,52] The line-of-sight integrated OH[*] chemiluminescence is used as an HRR proxy.[61,62] Then, the Pearson correlation between the time series of intensity fluctuations obtained from the OH[*] chemiluminescence images is calculated. A link between each pair of nodes (grid point locations x_i and x_j) is established with a strength corresponding to the Pearson correlation value between HRR signals $q'(t)_i$ and $q'(t)_j$ at these locations. As such, the adjacency matrix element R_{ij} of the HRR network is defined as

$$R_{ij}(t) = \frac{\sum_{t=1}^{n}\left(q'(t)_i - \overline{q'}_i\right)\left(q'(t)_j - \overline{q'}_j\right)}{\sqrt{\sum_{t=1}^{n}\left(q'(t)_i - \overline{q'}_i\right)^2}\sqrt{\sum_{t=1}^{n}\left(q'(t)_j - \overline{q'}_j\right)^2}}, \quad (3)$$

which is calculated over its preceding $n = 50$ time steps. $\overline{q'}_i$ and $\overline{q'}_j$ denotes the temporal mean of $q'(t)_i$ and $q'(t)_j$ across n time steps, respectively. This is equivalent to applying a sliding time window onto the transient HRR field. Here, n is chosen based on approximately one cycle of PVC oscillation to filter out turbulent noises. However, n cannot be too large so as to avoid excessive time-averaging effects.[51,52] Note that although R_{ij} is obtained based on time-averaging, the resultant network is time-varying since the calculation is updated at every time step.

A positive R_{ij} suggests that the variations of both time series are in phase, while a negative R_{ij} indicates that the variation of one time series is out of phase with the other. $R_{ij} = 0$ means there is no correlation between the two time series within the considered time interval. To separate the in-phase and out-of-phase correlations, we define two new positive and negative adjacency matrices, A_H^+ and A_H^-, as

$$A_{H_{ij}}^+(t) = \begin{cases} W_{ij} = R_{ij}(t), & \text{if } R_{ij} \geq \varepsilon, \\ W_{ij} = 0, & \text{otherwise}, \end{cases} \quad (4)$$

$$A_{H_{ij}}^-(t) = \begin{cases} W_{ij} = -R_{ij}(t), & \text{if } -R_{ij} \geq \varepsilon, \\ W_{ij} = 0, & \text{otherwise.} \end{cases} \quad (5)$$

Here, $\varepsilon = 0.4$ is a prescribed threshold used to screen out weak correlations and noises. Since Pearson correlation is a commutative operation, it automatically ensures that the HRR networks are undirected and without self-loops.

C. Key network parameters

Given the adjacency matrices, we can proceed to analyze the characteristic network structure parameters, including the degree k_i, the node strength s_i, and the average degree $k_{nn,i}$ (i is the node index) to study the network topologies of different flames in the vortical and HRR networks. k_i quantifies the number of nodes connected to node i as $k_i = \sum_{j=1}^{N} nnz(A_{ij})$, where nnz is the number of non-zero elements in the ith row of the adjacency matrix A with N being the total number of network nodes. s_i denotes the sum of the weights of all links to node i, calculated as $s_i = \sum_{j=1}^{N}(A_{ij})$. Both k_i and s_i quantify the relative importance of node i in the network. Their corresponding probability distribution functions, $P(k)$ and $P(s)$, characterize the scale-free feature of the networks.[44,47,51,53] Here, $P(k)$ and $P(s)$ are computed as $P(k) = n_k/N$ and $P(s) = n_s/N$, respectively, with n_k and n_s being the numbers of nodes with degree k and node strength s, respectively.

The importance of a node depends largely on its spatial location, which could influence its interactions with the neighboring nodes reflected by the degree correlations in the network.[51] To this end, the effect of neighboring nodes can be evaluated by the average degree of the nearest neighboring nodes[63] of node i as $k_{nn,i} = \frac{1}{k_i} \sum_{j \in \Omega(i)} k_j$, where $\Omega(i)$ represents the ensemble of node i's nearest neighboring nodes (nn). Then, the degree correlation function, $k_{nn}(k)$, is calculated as $k_{nn}(k) = \sum_{k'} k' P(k'|k)$, where $P(k'|k)$ is the conditional probability of a k-degree node being connected to a k'-degree node. Thus, $k_{nn}(k)$ can be understood as the average degree of the neighboring node of all k-degree nodes.

IV. RESULTS AND DISCUSSION

A. Helical flame in transition

In this study, the effect of PVC is investigated based on a distinct transitioning helical flame between symmetric and helical states, which enables the comparative study between the two states with and without PVC for a given flame condition. This flame emerges within a narrow range of operation conditions near the lean blowout limit (LBO) at a relatively low Re ranging between 2000 and 3500, as shown in Fig. 2. Experimentally, this flame can be obtained by decreasing Φ of an attached symmetric V-shaped flame at a fixed Re. The transition boundaries in Fig. 2 are then identified, with each data point determined based on three repeated tests.

The characteristics of such flame dynamics are next analyzed for a representative case with $Re = 2500$ and $\Phi = 0.52$, based on time series data containing 4972 snapshots of SPIV and OH* chemiluminescence images, corresponding to a duration of 497.2 ms. We first provide a general understanding of the two individual flame modes by comparing their transient flame and flow structures in Figs. 3(a) and 3(b). It is seen that the flame in the symmetric mode is attached to the bluff body tip on the bottom, whereas the helical flame is lifted by
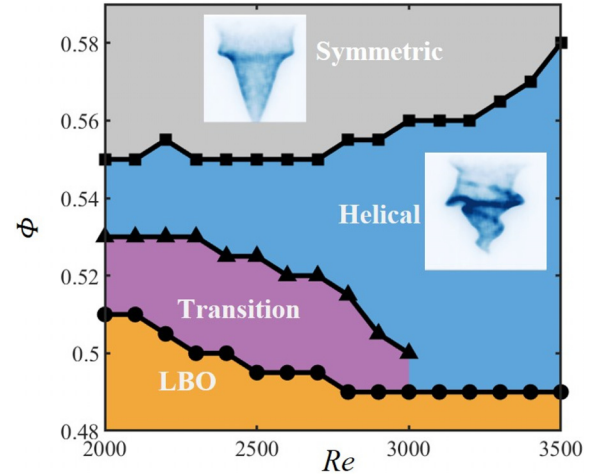

FIG. 2. Regime diagram of attached symmetric flame and lifted helical flame near the LBO.

about 10 mm above the nozzle exit. For the latter, the flame is anchored to a stagnation point, which is situated within the inner shear layer (ISL) and revolves periodically around the center axis. Furthermore, the overlapped Q-criterion[64] contours in Fig. 3(b) exhibit a distinct zig-zag vortex pattern along the ISL, which closely twines around the spiral-shaped flame surface in the near field, manifesting the typical characteristics of a PVC. In contrast, no such vortex is present in the symmetric flame. However, both flames feature large-scale symmetric vortex arrays in the outer shear layer (OSL), namely, the outer vortex rings (OVRs), which are responsible for the large amplitude flame surface deformation in the far field. It should be noted that the emergence of PVC in the present flame is independent of the existence of an apparent central recirculation zone (CRZ), which is normally associated with vortex breakdown at a high swirl number. However, our result suggests that the generation of PVC is not limited to flames of strong swirl intensity.

The transition between the symmetric and helical modes is demonstrated in Fig. 3(c), which is characterized by a flame root intensity, I_{root}, defined as the integration of the OH* signal over a prescribed zone near the burner exit [encircled by the dotted orange rectangles in Figs. 3(a) and 3(b)]. With I_{root} normalized to the range [0, 1], we identify the flame with $I_{root} \geq 0.9$ as the symmetric mode, which corresponds to a fully attached symmetric flame. Conversely, the flame with $I_{root} < 0.9$ is identified as the helical mode as the flame becomes asymmetric once its base is lifted. Based on this criterion, we observe that the attached symmetric flame appears during $t_1 \sim t_2$ and $t_3 \sim t_4$, whereas the lifted helical flame prevails during the remaining time. Moreover, Fig. 3(c) also presents the time variation of the transverse velocity signal U_{ISL} in the vicinity of a PVC, representative of the flow oscillations in the ISL. U_{ISL} shown in Fig. 3(c) is normalized by its maximum value. We find that U_{ISL} surges when the flame is in the helical mode, which can be explained by the dramatic velocity fluctuation in the transverse direction caused by the presence of PVC.

Similar transition processes between lifted and attached swirling flames have also been reported in previous studies, which correlate this phenomenon to the change in the absolute hydrodynamic
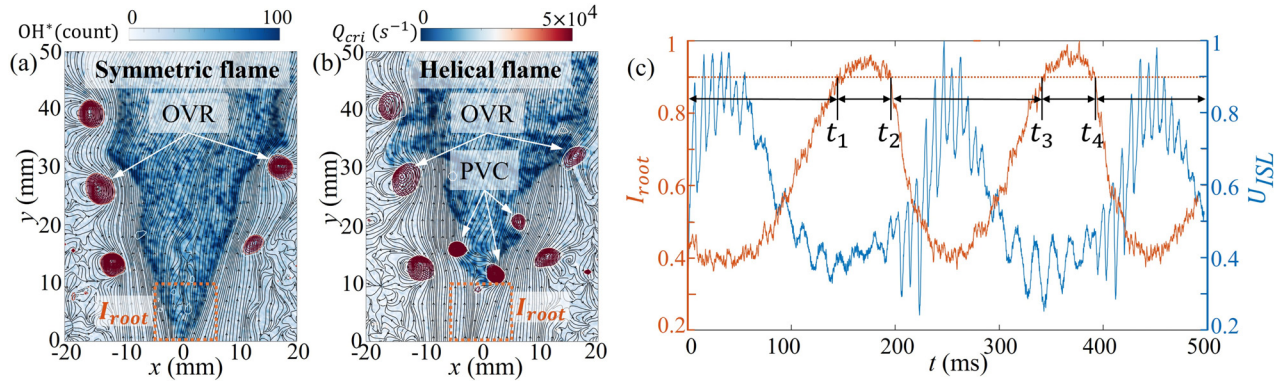
FIG. 3. Flame and vortex structures for (a) symmetric and (b) helical flame modes, characterized by OH* intensity and Q-criterion Q_{cri}, respectively. (c) Time variations of the transverse velocity in the ISL (probed at $x = 5.2$ mm and $y = 20$ mm) and the integrated OH* intensity I_{root} near the burner exit, with the integration windows marked by the dashed orange rectangles in (a) and (b). The dotted orange line in (c) corresponds to $I_{root} = 0.9$, below which we determine the flame to be in the lifted helical mode.

instabilities.[12,17,65,66] Here, we present the key snapshots of the flame and flow structures during the helical-to-symmetric and symmetric-to-helical transition processes in Fig. 4. The flame in Fig. 4(a) is initially in the helical state, with the lower stagnation point settled in the ISL at $y = 8$ mm. The PVC can be observed in the ISL, which is responsible for the zig-zag distortion of the flame root. According to previous works,[12,20,67,68] the presence of PVC is a manifestation of absolute instability in the helical mode. Then, the PVC gradually shrinks and diminishes, accompanied by the anti-streamwise movement of the flame's lower stagnation point and the disappearance of the twist of the flame root. Eventually, the stagnation point reattaches to the upstream bluff body and the flame reaches a fully symmetric state. According to previous studies,[12,23,69,70] this process is associated with an increased density gradient near the stagnation point, which leads to

the suppression of absolute instability. Conversely, the flame in Fig. 4(b) starts from the symmetric state with its root being slightly lifted and a weak PVC appearing near the flame root, owing to the onset of absolute instability. Then, the PVC undergoes a self-amplifying process and induces a zig-zag configuration of the flame root to form the helical mode, as the absolute instability develops. In a global instability sense, this self-exciting and self-amplifying process can be interpreted as an internal feedback mechanism originating from a region named the wavemaker. In this region, the flow-field perturbation can interact with the flame through density gradient variation, as has been demonstrated by previous works using LSA.[12,66,68,70]

To understand the mean flows with and without PVC, distributions of the time-averaged velocity components and the random mean square (RMS) δ of their fluctuation parts are plotted at four axial
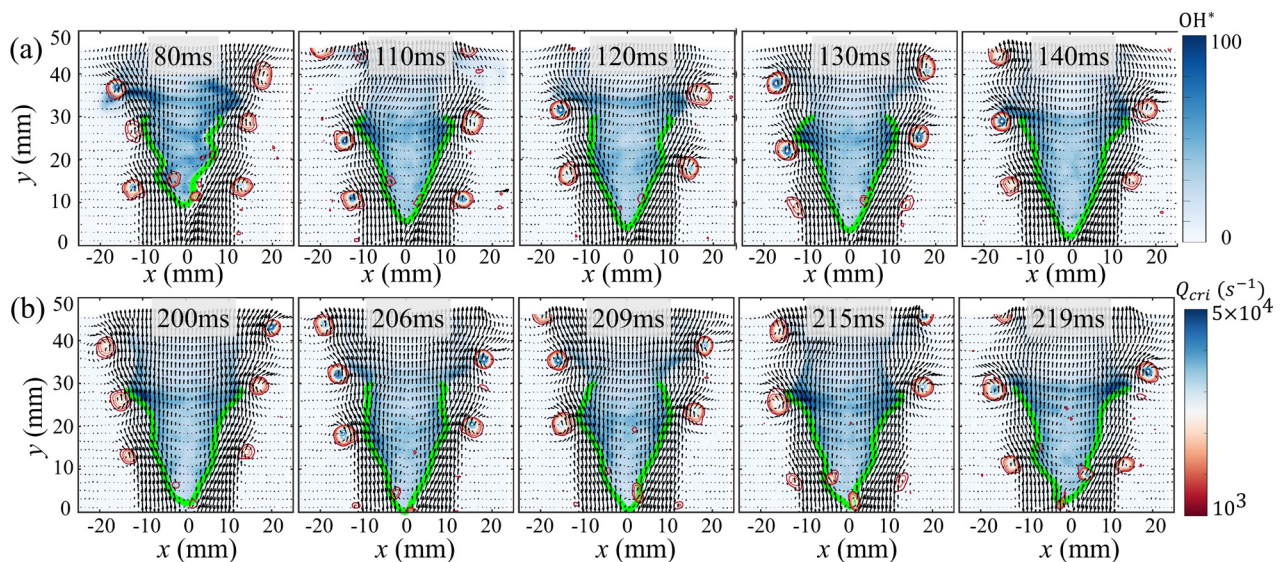

FIG. 4. Typical snapshots of flame and vortex structure propagation during (a) helical-to-symmetric flame and (b) symmetric-to-helical flame shape transition. Solid green lines indicate the flame edges with the Q-criterion Q_{cri} contours overlapped to indicate vortex structures.
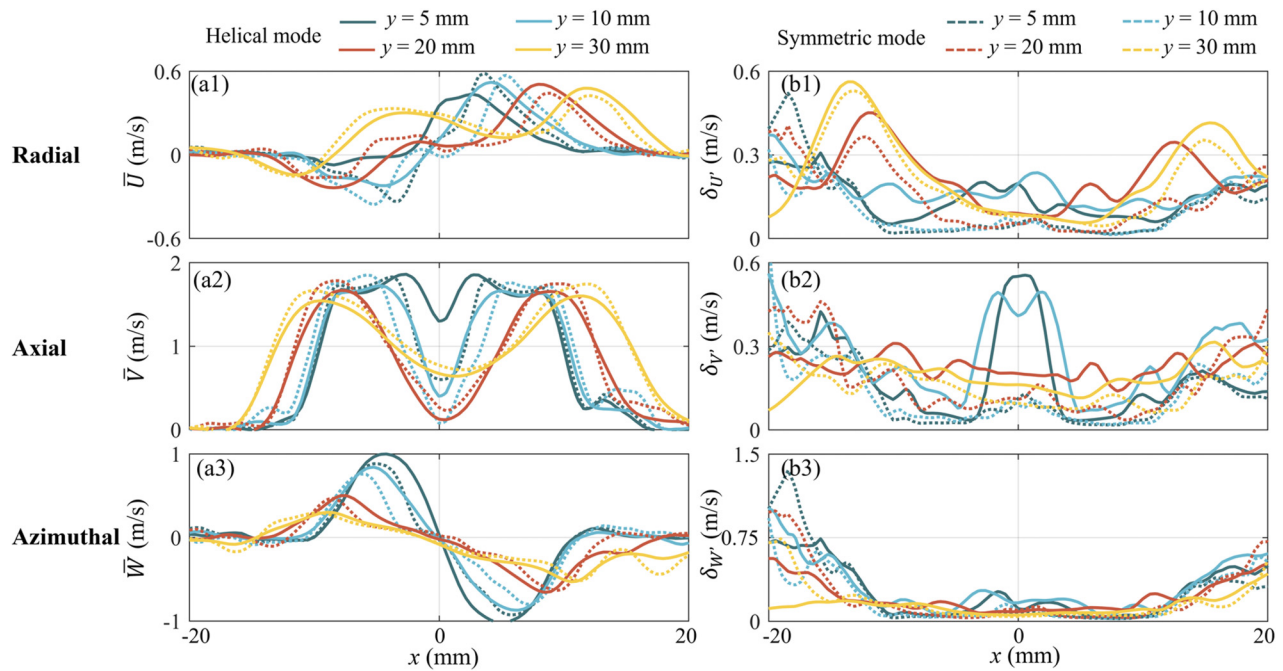
FIG. 5. Distributions of (a1)–(a3) the mean velocity components and (b1)–(b3) the corresponding RMS of the fluctuation parts at transverse planes of various heights ($y = 5$, 10, 20, and 30 mm). The mean fields are calculated based on data from t_2 to t_3 for the helical mode and data from t_1 to t_2 for the symmetric mode, respectively.

positions ($y = 5$, 10, 20, 30 mm) as shown in Figs. 5(a1)–5(a3) and 5(b1)–5(b3), respectively. The solid lines indicate results extracted from the helical mode during $t_2 \sim t_3$ with the existence of PVC, whereas the dotted lines indicate the symmetric mode during $t_1 \sim t_2$ without PVC. The velocity profiles share overall similarities between the two flame modes while several key distinctions exist. Close to the burner exit ($y = 5$ and 10 mm), the symmetric mode exhibits increased mean radial velocity component $\overline{U}$ compared with the helical mode. This disparity in the radial velocity likely reflects the thermal expansion effect, which causes radial acceleration of the burned gas in the flame root area in the symmetric mode. Additionally, at these lower locations, the helical mode demonstrates significantly elevated values of $\delta_{U'}$ near the centerline, which implies a vigorous radial oscillation induced by the PVC near the burner exit. For the axial velocity components in Figs. 5(a2) and 5(b2), the helical mode presents higher values of both $\overline{V}$ and $\delta_{V'}$ near the centerline at $y = 5$ and 10 mm, suggesting the effect of PVC in enhancing the mean and fluctuation of axial velocity near the burner exit region. The above results further corroborate the possible effect of PVC in initiating flame shape deformation and dynamics, owing to the enhanced local strain rate.[23,69] At downstream locations ($y = 20$ and 30 mm), the peak values of the mean and fluctuation parts of the radial and axial velocity components appear to occur at the OSL, further justifying the dominance of OVR in the far field. For the azimuthal components plotted in Figs. 5(a3) and 5(b3), the most discernible disparity can be observed at $y = 5$ and 10 mm, where the helical mode displays larger values of both average velocity $\overline{W}$ and fluctuation $\delta_{W'}$ near the centerline, compared with the symmetric mode. These discrepancies likely reflect the precession motion of the PVC.

B. Vortical network analysis

To understand the effects of the main coherent vortices, i.e., OVR and PVC, on the turbulence characteristics of the symmetric-helical transition process, we further perform a complex network analysis of vorticity (or turbulence) following the algorithm presented in our previous work.[53] We establish the network with the nodes being the elementary azimuthal vorticities, ω_z. The node strength s_i distribution is a key measure of vortical networks, which enables us to distinguish hubs that are crucial to the network connectivity.[44,50,52] Figures 6(a) and 6(b) present the instantaneous vorticity fields for the symmetric and helical flames, respectively, with the corresponding distributions of the node strength depicted in Figs. 6(c) and 6(d). We observe that the regions with high ω_z magnitude generally coincide well with those with high s values. This implies that the dominant vortical structures are responsible for creating clusters of strong nodes, which serve as hubs in the vortical network.

The node strength's probability distributions $P(s)$ are further plotted in Figs. 7(a) and 7(b). The power-law scaling $P(s) \sim s^{-\gamma}$ is confirmed for both distributions, with the scaling coefficient γ being 2.5 and 3.12 for the symmetric and helical flames. Note that γ is a key parameter assessing vortex interactions in the vortical network. Specifically, for $2 \leq \gamma \leq 3$, vortex interactions in turbulence can be characterized by a weighted scale-free network, which is resilient to perturbations imposed on randomly chosen nodes.[48,52,53] It follows that the symmetric flame with $\gamma = 2.5$ contains a broad range of scale-free vortical structures, which are not present for the helical flame.

Comparing Figs. 7(a) and 7(b), we find that the increase in γ in the helical flame can be directly attributed to the enhancement of a
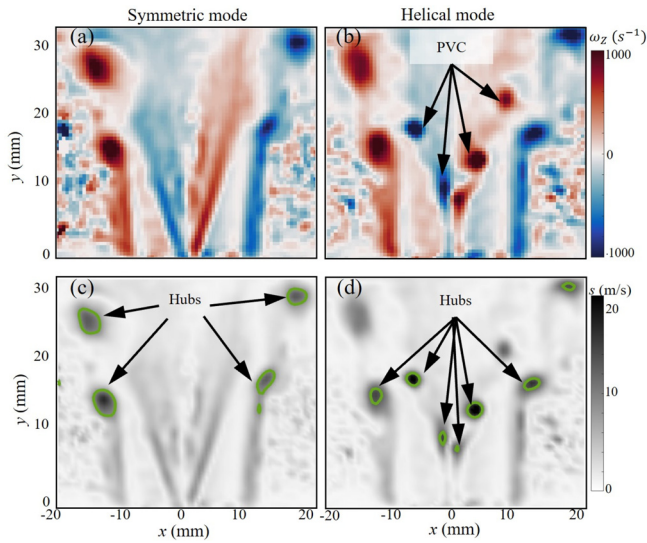
FIG. 6. (a)–(d) Vortical network analysis for transient symmetric (left) and helical (right) flames. (a) and (b) are the vorticity contours, (c) and (d) plot the node strength distributions, and the green lines in (c) and (d) indicate the upper limit contour of s satisfying the power-law fitting.

part of the medium-strength nodes, roughly corresponding to the s range of 5–10 m/s in the symmetric flame, which reduces the concentration of the medium-strength nodes while enriching the higher strength ones. This is also accompanied by the extension of the upper limit of the power-law fitting toward the high-strength end. Physically, this happens as the PVC emerges in the helical flame, leading to the formation of new hubs along the ISL shown in Fig. 6(d), which converts the turbulent structures in the ISL of the symmetric flame, consisting of medium-strength nodes, into coherent vortical structures of higher strength nodes. This is also consistent with our understanding that the appearance of coherent structures is destructive to the chaotic nature of turbulence, thereby driving the network away from the scale-free range.[53]

The time variation of the scaling coefficient γ throughout the transition period is plotted in Fig. 7(c). It shows exceptionally good correspondence between the time intervals with low γ and the symmetric flame. The same agreement can be confirmed between the intervals with $\gamma > 3$ and the helical flame, which accords with the observations from the transient results in Figs. 7(a) and 7(b). The field-averaged turbulence intensity $\tilde{\eta}_{tur}$ is overlapped in Fig. 7(c). Interestingly, it shows that the helical modes have higher turbulent intensity than the symmetric mode; however, the insight gained from the γ analyses in Figs. 7(a) and 7(b) suggest otherwise. This seeming paradox could arise from the calculation of $\tilde{\eta}_{tur}$, which does not
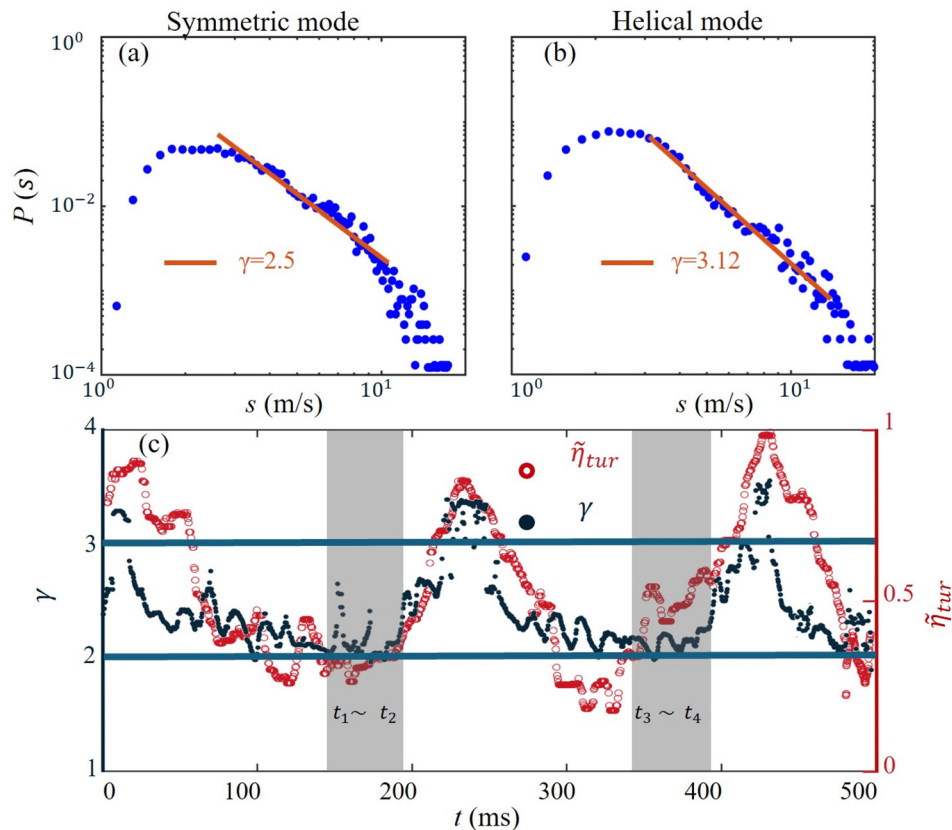

FIG. 7. Node strength distribution of vortical network for transient symmetric (left) and helical (right) modes. (a) and (b) show the power-law scaling of the node strength probability distribution, with a linear fitting slope of $-\gamma$. (c) plots the time variations of γ and the field-averaged turbulence intensity $\tilde{\eta}_{tur}$.

distinguish coherent fluctuation from random turbulence according to the classical triple decomposition.[71] Specifically, while the PVC can indeed enhance the overall fluctuation in the ISL, the enhanced part is primarily attributed to the coherent structures of high-degree order, and the contribution of the scale-free topology of the chaotic turbulence, which is of low-degree order, is suppressed. This can be also quantitatively seen in Fig. 6(d), where the low-s random hubs near the PVC are notably reduced compared with those in Fig. 6(c).

C. Heat release rate network analysis

Different from the turbulence network, complex networks of HRR can be constructed based on the temporal correlations among the nodes in the OH* intensity field. Examples of HRR networks have been introduced in the literature. Rywik *et al.*[52] found that the mean degree $\langle k \rangle$ of the HRR network is responsive to the changes in hydrogen fuel fraction and root mean square of acoustic pressure as well as the shifts in the dynamical state. Kasthuri *et al.*[51] confirmed a strong assortative mixing in the HRR networks during thermoacoustic instability by fitting the degree correlation functions $k_{nn}(k)$ to a power-law scaling. We next employ the positive and negative HRR networks to understand the effects of coherent structures on the HRR characteristics during the symmetric-helical flame transition.

The results for positive and negative networks are compared in Figs. 8(a)–8(d) for transient symmetric and helical flames. Basically, the k strength measures the temporal relevance of an HRR node to the entire field, which in a sense reflects the coherence of its related flame structure. Indeed, in comparing Figs. 8(a) to 8(d), we find the high-k regions are more extended in the helical flame than those in the symmetric flame. Furthermore, the high-k nodes tend to cluster near the OVR cores in the symmetric flame, whereas those in the helical

flame gather around both the PVC in the near field and the OVRs in the far field. These point to a strengthened connectivity of the HRR network brought about by the highly coherent PVC.

To further illustrate the differences in the spatial correlations of positive and negative HRR networks, the links from a representative high-strength node of a cluster to its correlated nodes are also displayed in Figs. 8(a)–8(d). The strong correlation between the HRR clusters and their nearby coherence vortices can be understood from the fact that the temporal features of the clusters are dominated by the periodic fluctuations of the flame surfaces, resulting from the periodic dynamics of the coherent vortices. As such, nodes' strengths varying in phase with each other are positively correlated, whereas those oscillating out of phase are negatively correlated. Thus, the links in positive networks are generally between the in-phase nodes, while the links in negative networks are between out-of-phase nodes. Specifically, for the symmetric flame in Figs. 8(a) and 8(b), the positive network links are established mostly within the same cluster or between the nodes of a symmetric pair of clusters in the vicinity of the OVRs. However, the correlated nodes in the negative network are slightly offset from the main clusters. Similar spatial connections can be found in the helical flame in Figs. 8(c) and 8(d), but with the correlated nodes distributed mainly within the PVC-dominating clusters. Again, this implies a decisive role of PVC in promoting the coherence of the HRR variation, especially in the near field.

Similar to the scaling analysis of the vortical network, we explore the power-law scaling of the HRR network based on the relationship between the degree correlation function $k_{nn}(k)$ and degree k in Figs. 9(a) and 9(b). For the positive networks in Fig. 9(a), the power-law scaling, $k_{nn}(k) \sim k^{\mu}$, can be observed for both symmetric and helical flames, with the goodness of fitting $R^2 > 0.9$ for both cases. Such strong positive degree–degree correlations imply a preference of the network for assortative mixing property, meaning that connections are established between nodes of similar degrees.[51,72] Physically, this assortative mixing can be attributed to the coherent structures, including OVR and PVC, which serve to sustain in-phase connections within the HRR network. The scaling coefficient μ, however, does not exhibit significant differences between the two flame modes. As for the negative networks in Fig. 9(b), the power-law scaling still exists for the helical flame; however, for $4 < \log(k) < 5$ in the symmetric case, $k_{nn}(k)$ decreases with increasing k, indicating a disassortative mixing property.[72] This can be explained by the distribution of the correlated nodes in Fig. 8(b), which shows a spatial shift of these nodes away from the coherent OVRs, thereby producing a diminished coherence of the out-of-phase HRR variation. Interestingly, this is not the case for the helical flame because an out-of-phase HRR variation can always be found in a PVC-adjacent flame surface, as the spiral vortex can be considered an integration of vortices with phases varying continuously in the axial direction.

Based on the above results, we find that, for the positive network, the node degree distribution of the helical flame is concentrated more on the high-k end compared with the symmetric flame, implying a larger mean degree $\langle k \rangle_{pos}$. To this end, $\langle k \rangle_{pos}$ may be used as another measure distinguishing symmetric and helical flames. Furthermore, the effect of the PVC's presence on the network's assortativity is indicated by the goodness R^2_{neg} of the power-law fitting in the negative network, which may also serve to differentiate the two different flames. To check their performances, the time
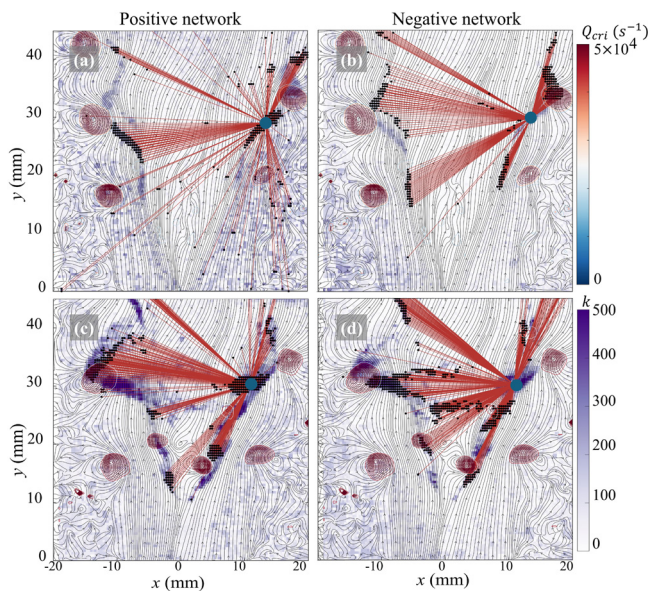

FIG. 8. (a)–(d) Positive (left) and negative (right) HRR network analysis for transient symmetric and helical flames. The distributions of network degree k are plotted for (a) and (b) symmetric and (c) and (d) helical flames. The links connect a representative high-strength node (blue dot) to its correlated nodes (black dots).
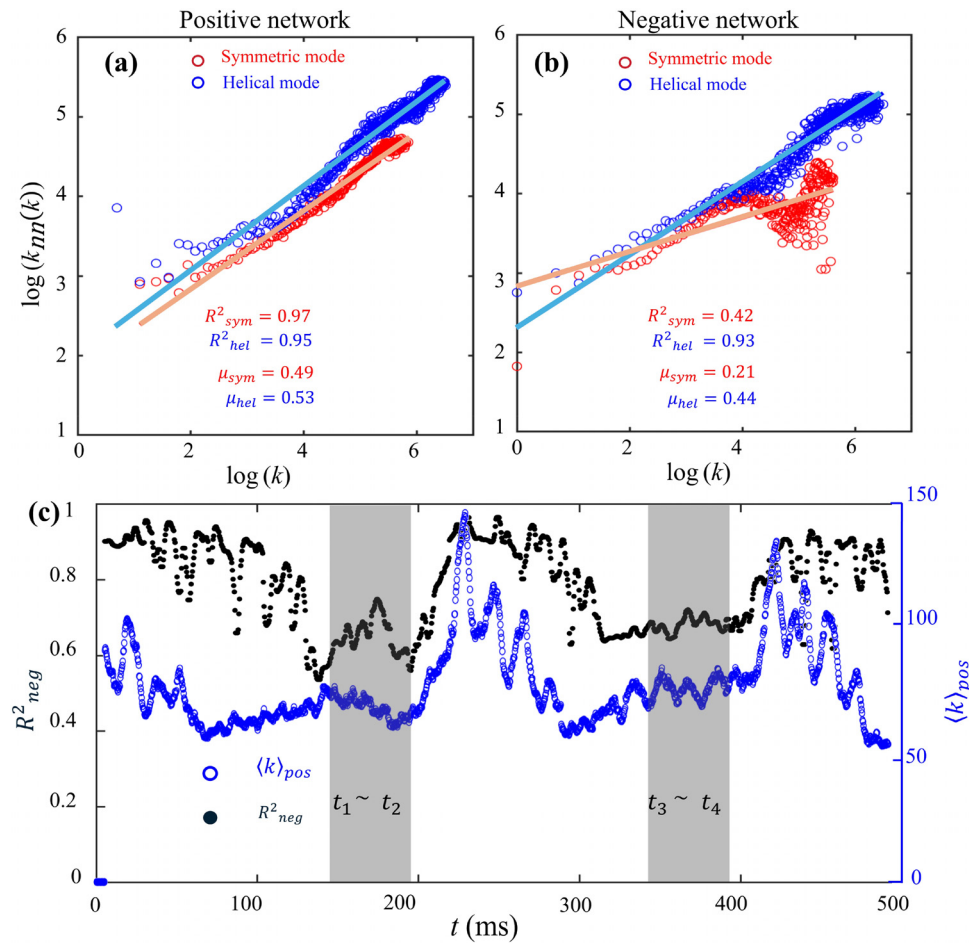
FIG. 9. (a) and (b) compare the power-law scaling of the corresponding degree correlation function $k_{nn}(k)$ vs k, together with linear fitting slope μ and goodness R^2. (c) plots the time variations of the mean degree $\langle k \rangle_{pos}$ of positive networks and the goodness of fitting R^2_{neg} of negative networks.

variations of $\langle k \rangle_{pos}$ and R^2_{neg} are plotted in Fig. 9(c) for the entire transition process, displaying a qualitative agreement of the symmetric flame periods with the troughs of both curves and agreement of the helical mode with the peaks. In short, the present analysis demonstrates that the effect of PVC on the HRR networks is primarily through improving the coherence of the flame surface's HRR variation. Combined with the vortical network analysis, the improved coherence in heat release oscillation likely results from the enhanced coherent fluctuation in the ISL.

V. CONCLUDING REMARKS

This work employed a 10-kHz simultaneous measurement of OH^* chemiluminescence and SPIV to study the effect of PVC on the vortical and HRR network structures of a weak premixed swirling flame, based on a unique transitioning flame switching between a lifted helical mode and an attached symmetric mode. During the flame shape transition, PVC appears and vanishes alternately in a quasi-periodic manner, respectively synchronizing with the lifting and reattaching processes of the flame root. To quantitatively assess

the key correlations and network topologies in the PVC–flame interaction, we developed both vortical and HRR networks based on the time-resolved vorticity and HRR fields, respectively. We found that the node strength in the vortical network exhibits power-law scaling for an extended range of node strength. The scale-free topology, which is characteristic of the vortex interactions in a turbulent flow, can be confirmed for the symmetric flame with the coherent OVRs acting as hubs. However, this scale-free feature breaks for the lifted helical flame, owing to the significantly enhanced coherence of the flow oscillation in the ISL induced by PVC. In the HRR networks, we observed the formation of high-degree clusters as the flame surfaces fluctuate periodically, which results from the periodic dynamics of the coherent vortices. In particular, the PVC promotes coherence in the local HRR variation, especially in the near field, leading to an enhancement in the mean degree of positive networks and an assortative mixing in the negative networks. These results have important implications for the development of combustion control strategies based on network theory, as the system dynamics could be dramatically altered in the presence of PVC.

AUTHOR DECLARATIONS
Conflict of Interest

The authors have no conflicts to disclose.

Author Contributions

Yongzhi Ren: Data curation (lead); Investigation (lead); Writing – original draft (lead). **Qiuxiao Wang:** Data curation (supporting); Investigation (supporting); Validation (supporting). **Yu Guan:** Validation (lead); Writing – review & editing (supporting). **Xi Xia:** Conceptualization (lead); Supervision (equal); Writing – review & editing (lead). **Fei Qi:** Methodology (equal); Resources (equal); Supervision (equal).

DATA AVAILABILITY

The data that support the findings of this study are available from the corresponding authors upon reasonable request.

REFERENCES

[1]H. Mongia, "TAPS: A fourth generation propulsion combustor technology for low emissions," AIAA Paper No. 2003-2657, 2003.

[2]E. Mastorakos, "Forced ignition of turbulent spray flames," Proc. Combust. Inst. **36**, 2367 (2017).

[3]Y. Liu, X. Sun, V. Sethi, D. Nalianda, Y.-G. Li et al., "Review of modern low emissions combustion technologies for aero gas turbine engines," Prog. Aerosp. Sci. **94**, 12 (2017).

[4]J. E. Temme, P. M. Allison, and J. F. Driscoll, "Combustion instability of a lean premixed prevaporized gas turbine combustor studied using phase-averaged PIV," Combust. Flame **161**, 958 (2014).

[5]M. Foust, D. Thomsen, R. Stickles, C. Cooper, and W. Dodds, "Development of the GE aviation low emissions TAPS combustor for next generation aircraft engines," AIAA Paper No. 2012-0936, 2012.

[6]A. Huonder and D. Olsen, "Methane emission reduction technologies for natural gas engines: A review," Energies **16**, 7054 (2023).

[7]K. Oberleithner, C. O. Paschereit, and I. Wygnanski, "On the impact of swirl on the growth of coherent structures," J. Fluid Mech. **741**, 156 (2014).

[8]S. Candel, D. Durox, T. Schuller, J.-F. Bourgouin, and J. P. Moeck, "Dynamics of swirling flames," Annu. Rev. Fluid Mech. **46**, 147 (2014).

[9]D. G. Lilley, "Swirl flows in combustion: A review," AIAA J. **15**, 1063 (1977).

[10]D. Durox, T. Schuller, N. Noiray, and S. Candel, "Experimental analysis of nonlinear flame transfer functions for different flame geometries," Proc. Combust. Inst. **32**, 1391 (2009).

[11]G. Wang, X. Liu, X. Xia, S. Wang, and F. Qi, "Dynamics of periodically-excited vortices in swirling flames," Proc. Combust. Inst. **38**, 6183 (2021).

[12]K. Oberleithner, M. Stöhr, S. H. Im, C. M. Arndt, and A. M. Steinberg, "Formation and flame-induced suppression of the precessing vortex core in a swirl combustor: Experiments and linear stability analysis," Combust. Flame **162**, 3100 (2015).

[13]S. Terhaar, K. Oberleithner, and C. O. Paschereit, "Key parameters governing the precessing vortex core in reacting flows: An experimental and analytical study," Proc. Combust. Inst. **35**, 3347 (2015).

[14]Y. Huang and V. Yang, "Dynamics and stability of lean-premixed swirl-stabilized combustion," Prog. Energy Combust. Sci. **35**, 293 (2009).

[15]N. Syred, "A review of oscillation mechanisms and the role of the precessing vortex core (PVC) in swirl combustion systems," Prog. Energy Combust. Sci. **32**, 93 (2006).

[16]K. Oberleithner, M. Sieber, C. N. Nayeri, C. O. Paschereit, C. Petz et al., "Three-dimensional coherent structures in a swirling jet undergoing vortex breakdown: Stability analysis and empirical mode construction," J. Fluid Mech. **679**, 383 (2011).

[17]K. Manoharan, M. Frederick, S. Clees, J. O'Connor, and S. Hemchandra, "A weakly nonlinear analysis of the precessing vortex core oscillation in a variable swirl turbulent round jet," J. Fluid Mech. **884**, A29 (2020).

[18]J. Zhang, X. Hui, Q. An, and A. M. Steinberg, "Transient dynamics of the precessing vortex core in an intermittently shape-transitioning swirl flame," Combust. Flame **250**, 112652 (2023).

[19]M. Stöhr, K. Oberleithner, M. Sieber, Z. Yin, and W. Meier, "Experimental study of transient mechanisms of bistable flame shape transitions in a swirl combustor," J. Eng. Gas Turbines Power **140**, 011503 (2018).

[20]P. Meliga, F. Gallaire, and J.-M. Chomaz, "A weakly nonlinear mechanism for mode selection in swirling jets," J. Fluid Mech. **699**, 216 (2012).

[21]S. Gupta, A. Datta, S. Hemchandra, and I. Boxx, "Precessing vortex core suppression in a swirl stabilized combustor with hydrogen addition," in Proceedings of the ASME Turbo Expo 2023: Turbomachinery Technical Conference and Exposition. Volume 3A: Combustion, Fuels, and Emissions (American Society of Mechanical Engineers, 2023), p. V03AT04A002.

[22]G. Vignat, D. Durox, A. Renaud, T. Lancien, R. Vicquelin et al., "Investigation of transient PVC dynamics in a strongly swirled spray flame using high speed planar laser imaging of SnO_2 microparticles," Combust. Flame **225**, 305 (2021).

[23]Q. An and A. M. Steinberg, "The role of strain rate, local extinction, and hydrodynamic instability on transition between attached and lifted swirl flames," Combust. Flame **199**, 267 (2019).

[24]S. Taamallah, S. J. Shanbhogue, and A. F. Ghoniem, "Turbulent flame stabilization modes in premixed swirl combustion: Physical mechanism and Karlovitz number-based criterion," Combust. Flame **166**, 19 (2016).

[25]J. P. Moeck, J.-F. Bourgouin, D. Durox, T. Schuller, and S. Candel, "Nonlinear interaction between a precessing vortex core and acoustic oscillations in a turbulent swirling flame," Combust. Flame **159**, 2650 (2012).

[26]A. Renaud, S. Ducruix, P. Scouflaire, and L. Zimmer, "Flame shape transition in a swirl stabilised liquid fueled burner," Proc. Combust. Inst. **35**, 3365 (2015).

[27]S. Wang, J. Zheng, L. Xu, Q. An, X. Han et al., "Experimental investigation of the helical mode in a stratified swirling flame," Combust. Flame **244**, 112268 (2022).

[28]M. Stöhr, I. Boxx, C. Carter, and W. Meier, "Dynamics of lean blowout of a swirl-stabilized flame in a gas turbine model combustor," Proc. Combust. Inst. **33**, 2953 (2011).

[29]Q. An, W. Y. Kwong, B. D. Geraedts, and A. M. Steinberg, "Coupled dynamics of lift-off and precessing vortex core formation in swirl flames," Combust. Flame **168**, 228 (2016).

[30]F. Lückoff and K. Oberleithner, "Excitation of the precessing vortex core by active flow control to suppress thermoacoustic instabilities in swirl flames," Int. J. Spray Combust. Dyn. **11**, 175682771985623 (2019).

[31]M. Frederick, K. Manoharan, J. Dudash, B. Brubaker, S. Hemchandra et al., "Impact of precessing vortex core dynamics on shear layer response in a swirling jet," J. Eng. Gas Turbines Power **140**, 061503 (2018).

[32]S. Wang, J. Zheng, L. Li, Z. Yang, X. Xia et al., "Evolution characteristics of 3D vortex structures in stratified swirling flames studied by dual-plane stereoscopic PIV," Combust. Flame **237**, 111874 (2022).

[33]J. P. Moeck, J.-F. Bourgouin, D. Durox, T. Schuller, and S. Candel, "Tomographic reconstruction of heat release rate perturbations induced by helical modes in turbulent swirl flames," Exp. Fluids **54**, 1498 (2013).

[34]B. D. Geraedts, C. M. Arndt, and A. M. Steinberg, "Rayleigh index fields in helically perturbed swirl-stabilized flames using doubly phase conditioned OH* chemiluminescence tomography," Flow. Turbul. Combust. **96**, 1023 (2016).

[35]A. M. Steinberg, I. Boxx, M. Stöhr, C. D. Carter, and W. Meier, "Flow–flame interactions causing acoustically coupled heat release fluctuations in a thermoacoustically unstable gas turbine model combustor," Combust. Flame **157**, 2250 (2010).

[36]A. Datta, S. Gupta, I. Chterev, I. Boxx, and S. Hemchandra, "Impact of hydrogen addition on the thermoacoustic instability and precessing vortex core

dynamics in a CH_4/H_2/air technically premixed combustor," J. Eng. Gas Turbines Power **144**, 021013 (2022).

[37] A. M. Steinberg, I. Boxx, M. Stohr, W. Meier, and C. D. Carter, "Effects of flow structure dynamics on thermoacoustic instabilities in swirl-stabilized combustion," AIAA J. **50**, 952 (2012).

[38] B. Zhang, M. Shahsavari, Z. Rao, S. Yang, and B. Wang, "Thermoacoustic instability drivers and mode transitions in a lean premixed methane-air combustor at various swirl intensities," Proc. Combust. Inst. **38**, 6115 (2021).

[39] P. M. Anacleto, E. C. Fernandes, M. V. Heitor, and S. I. Shtork, "Swirl flow structure and flame characteristics in a model lean premixed combustor," Combust. Sci. Technol. **175**, 1369 (2003).

[40] Y. Mori, T. Kawada, S. Fukuda, and H. Gotoda, "Nonlinear dynamics of attenuation behavior in combustion oscillations in a swirl-stabilized combustor," Proc. Combust. Inst. **39**, 4671 (2023).

[41] A. Roy, S. Singh, A. Nair, S. Chaudhuri, and R. Sujith, "Flame dynamics during intermittency and secondary bifurcation to longitudinal thermoacoustic instability in a swirl-stabilized annular combustor," Proc. Combust. Inst. **38**, 6221 (2021).

[42] A. Towne, O. T. Schmidt, and T. Colonius, "Spectral proper orthogonal decomposition and its relationship to dynamic mode decomposition and resolvent analysis," J. Fluid Mech. **847**, 821 (2018).

[43] G. Iacobello, L. Ridolfi, and S. Scarsoglio, "A review on turbulent and vortical flow analyses via complex networks," Phys. Stat. Mech. Appl. **563**, 125476 (2021).

[44] K. Taira and A. G. Nair, "Network-based analysis of fluid flows: Progress and outlook," Prog. Aerosp. Sci. **131**, 100823 (2022).

[45] R. I. Sujith and V. R. Unni, "Dynamical systems and complex systems theory to study unsteady combustion," Proc. Combust. Inst. **38**, 3445 (2021).

[46] S. Murayama, K. Kaku, M. Funatsu, and H. Gotoda, "Characterization of dynamic behavior of combustion noise and detection of blowout in a laboratory-scale gas-turbine model combustor," Proc. Combust. Inst. **37**, 5271 (2019).

[47] M. Murugesan and R. I. Sujith, "Combustion noise is scale-free: Transition from scale-free to order at the onset of thermoacoustic instability," J. Fluid Mech. **772**, 225 (2015).

[48] R. I. Sujith and V. R. Unni, "Complex system approach to investigate and mitigate thermoacoustic instability in turbulent combustors," Phys. Fluids **32**, 061401 (2020).

[49] A. G. Nair and K. Taira, "Network-theoretic approach to sparsified discrete vortex dynamics," J. Fluid Mech. **768**, 549 (2015).

[50] K. Taira, A. G. Nair, and S. L. Brunton, "Network structure of two-dimensional decaying isotropic turbulence," J. Fluid Mech. **795**, R2 (2016).

[51] P. Kasthuri, A. Krishnan, R. Gejji, W. Anderson, N. Marwan et al., "Investigation into the coherence of flame intensity oscillations in a model multi-element rocket combustor using complex networks," Phys. Fluids **34**, 034107 (2022).

[52] M. Rywik, P. Kasthuri, I. Boxx, I. Chterev, W. Polifke et al., "Turbulence and heat release rate network structure in hydrogen-enriched combustion," Proc. Combust. Inst. **39**, 4701 (2023).

[53] J. Zheng, Y. Guan, L. Xu, X. Xia, L. K. B. Li et al., "Scale-free topology of vortical networks in a turbulent thermoacoustic system," Phys. Rev. Fluids **9**, 033202 (2024).

[54] Q. Wang, Y. Ren, M. Gu, B. Yu, X. Feng et al., "Influence of inner shear layer on the emergence of central recirculation zone in a V-shaped premixed swirling flame," Phys. Fluids **35**, 107129 (2023).

[55] Z. Li, L. Huang, X. Zhou, X. Huang, Z. Chen et al., "Scaling up in situ combustion process for enhanced oil recovery in water-flooded light oil reservoirs from laboratory to field implementation," Phys. Fluids **36**, 037140 (2024).

[56] L. Huang, Z. Li, Y. Wang, L. Zhang, Y. Su et al., "Experimental assessment on the explosion pressure of CH_4-air mixtures at flammability limits under high pressure and temperature conditions," Fuel **299**, 120868 (2021).

[57] A. K. Prasad and K. Jensen, "Scheimpflug stereocamera for particle image velocimetry in liquid flows," Appl. Opt. **34**, 7092 (1995).

[58] B. Wieneke, "Stereo-PIV using self-calibration on particle images," Exp. Fluids **39**, 267 (2005).

[59] A. Krishnan, R. I. Sujith, N. Marwan, and J. Kurths, "On the emergence of large clusters of acoustic power sources at the onset of thermoacoustic instability in a turbulent combustor," J. Fluid Mech. **874**, 455 (2019).

[60] S. Murayama, H. Kinugawa, I. T. Tokuda, and H. Gotoda, "Characterization and detection of thermoacoustic combustion oscillations based on statistical complexity and complex-network theory," Phys. Rev. E **97**, 022223 (2018).

[61] X. Liang, Z. Wang, L. Ji, L. Yang, and J. Li, "Comparisons between the disturbances in chemiluminescence and heat release rate from acoustically perturbed partially premixed and diffusion flames," Phys. Fluids **36**, 023621 (2024).

[62] Y. Yang, G. Wang, Y. Fang, T. Jin, and J. Li, "Experimental study of the effect of outlet boundary on combustion instabilities in premixed swirling flames," Phys. Fluids **33**, 027106 (2021).

[63] A. Barrat, M. Barthélemy, and A. Vespignani, "The effects of spatial constraints on the evolution of weighted complex networks," J. Stat. Mech. **2005**, P05003.

[64] Y. Dubief and F. Delcayre, "On coherent-vortex identification in turbulence," J. Turbul. **1**, N11 (2000).

[65] S. Terhaar, B. Ćosić, C. O. Paschereit, and K. Oberleithner, "Suppression and excitation of the precessing vortex core by acoustic velocity fluctuations: An experimental and analytical study," Combust. Flame **172**, 234 (2016).

[66] L. Rukes, M. Sieber, C. O. Paschereit, and K. Oberleithner, "The impact of heating the breakdown bubble on the global mode of a swirling jet: Experiments and linear stability analysis," Phys. Fluids **28**, 104102 (2016).

[67] L. Rukes, M. Sieber, C. O. Paschereit, and K. Oberleithner, "Transient evolution of the global mode in turbulent swirling jets: Experiments and modal stability analysis," Eur. J. Mech. B **65**, 98 (2017).

[68] F. Gallaire and J.-M. Chomaz, "Mode selection in swirling jet experiments: A linear stability analysis," J. Fluid Mech. **494**, 223 (2003).

[69] Q. An, W. Y. Kwong, B. D. Geraedts, and A. M. Steinberg, "Coupled dynamics of lift-off and precessing vortex core formation in swirl flames," Combust. Flame **168**, 228 (2016).

[70] J. Zhang, X. Hui, Q. An, and Z. Wang, "Impact of density stratification and azimuthal velocity on the growth of coherent structures in a convectively unstable swirl flame," Phys. Fluids **35**, 105149 (2023).

[71] A. K. M. F. Hussain and W. C. Reynolds, "The mechanics of an organized wave in turbulent shear flow," J. Fluid Mech. **41**, 241 (1970).

[72] M. E. J. Newman, "Assortative mixing in networks," Phys. Rev. Lett. **89**, 208701 (2002).

28 November 2025 07:58:47